

Bifurcations in a controlled system with softening stiffness

The Virtual Mechanical System control law for nonlinear vibration control

Sarah Geyskens^{1*}, Jasper Juchem¹, Kevin Dekemele¹,
Mia Loccufier¹

¹Dept. of Electromechanical, Systems and Metal Engineering, Research group Dynamical Systems and Control (DySC), Ghent University, Tech lane, Ghent, 9052, Belgium.

*Corresponding author(s). E-mail(s): Sarah.Geyskens@UGent.be;

Abstract

This study investigates the control of an impulsively excited one-degree-of-freedom (DOF) oscillator with softening stiffness, modelled with an arctangent characteristic. The goal is to control the host system's vibrations by transferring the vibrational energy to an active controller. To this end, a Virtual Mechanical System (VMS) control law is implemented. This law is characterised by controller dynamics, which describe the behaviour of a mechanical system coupled to the host system skew-symmetrically in the velocities and having stiffness identical to that of the host system. The hypothesis is that this similarity and unique coupling facilitate energy transfer. By using the Complexification-Averaging (CxA) technique and examining the slow flow dynamics wrt. fixed points, bifurcations and impulsive orbits, the conditions for energy transfer are uncovered, enabling tuning of the controller.

Keywords: Nonlinear dynamics, Bifurcations, Energy threshold, Passivity based control, Active vibration control

1 Introduction

Nonlinear dynamical systems exhibit complex behaviours that can pose challenges regarding control and stability [1, 2]. In particular, active feedback control strategies, while effective in many scenarios, can introduce instabilities under certain conditions. Passivity-Based Control (PBC) provides a robust methodology to address these challenges. The PBC framework, comprising interconnected passive dynamical systems, inherently preserves passivity, ensuring input-output stability [3]. Various PBC strategies have been developed [4–8].

In this work, a passive single-degree-of-freedom (SDOF) nonlinear oscillator (host) is coupled to a passivity-based active controller, referred to as the Virtual Mechanical System (VMS) because of the underlying Euler-Lagrange model that yields the control force. This controller was first introduced in [9], based on the work of L. Luyckx et al. [10]. The host’s nonlinearity is a softening stiffness nonlinearity, modelled as an arctangent, to portray saturation.

This type of stiffness characteristic is typical for constant force or constant torque mechanisms, which have applications in exoskeletons [11], aerospace [12], and robotic end-effectors like compliant fingers [13], grippers [14, 15] and polishing or deburring devices [16]. A softening stiffness is also used in passive vibration control [17, 18]. Different mechanisms have been designed to achieve this type of elastic force or torque [19–21]. This work offers insights into vibration control of systems with a softening stiffness characteristic when excited by an impulsive load.

The VMS control strategy differs from the previously mentioned PBC strategies as it describes an auxiliary structure which is excited by the velocity of the host and coupled to the host system skew-symmetrically [9]. This control loop is illustrated in Fig. 1. The unique skew-symmetric interconnection is conservative and ensures the preservation of passivity. The hypothesis is that the skew-symmetric coupling (with factor N), as seen in gyroscopic systems, facilitates energy transfer to the auxiliary system [9]. Note that the auxiliary system is virtual and only used to calculate the active control force, hence the name. Next to the stability property, another advantage is that well-developed techniques employed with passive vibration absorbers can be used to gain insights into the VMS tuning strategy. Here, as is the case in passive vibration absorbers, the principle of similarity is applied [22, 23], as the VMS copies the host’s nonlinear stiffness characteristic.

A key part of this study is the analysis of nonlinear phenomena, such as bifurcations. By leveraging nonlinear phenomena, such as nonlinear beating or internal resonance, energy displacement from host to VMS can be induced. Investigating this energy transfer is the main focus of this work.

The paper is structured as follows. In Section 2, the considered host system is defined. Furthermore, the equations of motion and controller dynamics are introduced. To facilitate the analytical investigation, the dimensionless equations are obtained in Sec. 2.1. Next, semi-analytical techniques are employed to analyse the dynamics. These tools enable the systematic investigation of energy transfer thresholds and provide insights into the underlying bifurcation mechanisms. Section 3 describes the complexification-averaging (CxA) analysis [24, 25]. Further, a bifurcation analysis is conducted in Section 4. The findings are visualised using impulsive orbits (IO) [26].

The results are presented and discussed in Section 5 and translated into a practical tuning strategy. By discussing trade-offs from a control perspective, a framework is provided for optimising the controller's performance. In Section 6, an illustrative example is given of how to apply this control strategy. Furthermore, by adding a damping term to the controller dynamics, the vibration energy is not only transferred but also dissipated. Finally, a conclusion is presented in Section 7.

Overall, this study contributes to the growing intersection of vibration control and nonlinear dynamics, offering a novel perspective on active control strategies and their potential to influence the energy distribution in nonlinear systems for practical advantage.

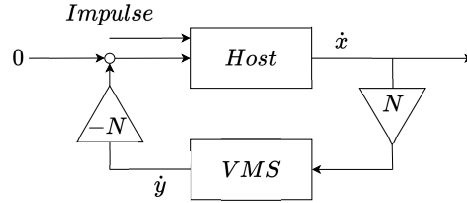


Fig. 1: Model of the active vibration control architecture with a VMS control law and impulse load

2 Model

As described before, the host system is a single-degree-of-freedom nonlinear system excited by an impulsive load. This is shown in Fig. 2a. The nonlinearity is embedded in the spring.

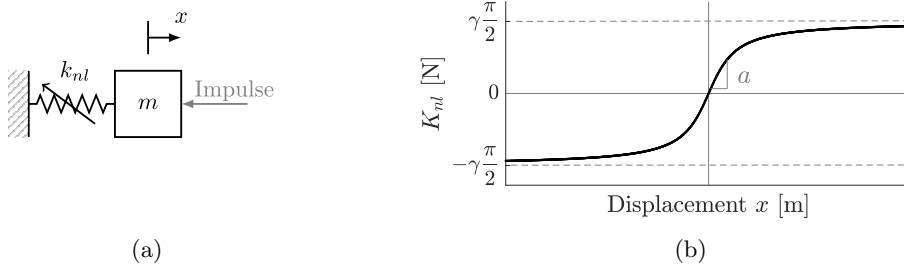


Fig. 2: a) A schematic of host system to be controlled, excited by an impulse load
b) The nonlinear elastic force characteristic of the host system, and mimicked in the controller dynamics

The equation of motion of the host system is

$$m \frac{d^2 x(t)}{dt^2} + \gamma \arctan \frac{a}{\gamma} x(t) + \epsilon a x(t) = F \delta(t), \quad (1)$$

where $m \in \mathbb{R}_{>0}$ is the mass with unit kilograms, $x \in \mathbb{R}$ is the displacement in metres, $K(x) = \gamma \arctan \frac{a}{\gamma} x + \epsilon a x$ represents the nonlinear stiffness force in Newton and $F \delta(t)$ is an external impulse load, which also has unit newton. The nonlinear elastic force $K(x)$ is defined by parameters $\gamma \in \mathbb{R}_{>0}$, with unit newton, and $a \in \mathbb{R}_{>0}$, with $[a] = \frac{N}{m}$. The nonlinear stiffness part is $K_{nl}(x) = \gamma \arctan \frac{a}{\gamma} x$. The characteristic of the nonlinear elastic force is depicted in Fig. 2b. As shown, γ determines that saturation force and a represents the slope of K_{nl} at the origin. The larger a , the steeper the arctangent characteristic is near the origin. This arctangent term is strongly nonlinear, and a small ($\epsilon = 0.01$) linear term is added to ensure the stiffness force does not saturate completely.

The VMS control law is applied to the host system as shown in Fig. 1. The controller adds dynamics to the system. The control force is obtained by evaluating an auxiliary structure (the VMS) which is excited by the velocity of the host and coupled to the host system skew-symmetrically [9]. To model this auxiliary system, the principle of similarity is applied [22, 23], as the VMS copies the host's nonlinear stiffness characteristic. The following equations of motion describe the host system and controller. Note that $-N \frac{dy(t)}{dt}$ is the control force and $F \delta(t)$ is an external impulse load, where $\delta(t)$ is the unit impulse.

$$\begin{cases} m \frac{d^2 x(t)}{dt^2} + \gamma \arctan \frac{a}{\gamma} x(t) + \epsilon a x(t) = -N \frac{dy(t)}{dt} + F \delta(t) \\ m \frac{d^2 y(t)}{dt^2} + \gamma \arctan \frac{a}{\gamma} y(t) + \epsilon a y(t) = N \frac{dx(t)}{dt} \end{cases} \quad (2)$$

Here, x represents the displacement of the main system and y represents the virtual displacement of the VMS control law. For brevity, the explicit time-dependence is omitted in the notation from here on. The host and controller are coupled skew-symmetrically in the velocities, with coupling parameter $N \in \mathbb{R}$. Due to the nature of the coupling between controller and host system, the combined system is stable, as proven in [9]. Note that the coupling is conservative, there are no dissipative terms in the equation of motion. The merit of this coupling is that it fundamentally changes the model structure. As in gyroscopic systems, the coupling induces a $\pm \frac{\pi}{2}$ phase shift between host and controller coordinates, which facilitates energy transfer [27].

2.1 Dimensionless system

In order to reduce the complexity of the analysis, dimensionless time and displacement are introduced. The dimensionless displacements are defined as $q = \alpha x$ and $z = \alpha y$, where $\alpha = \frac{a}{\gamma}$ and $[\alpha] = m^{-1}$. The dimensionless time is defined as $\tau = \beta t$, where $\beta = \sqrt{\frac{a}{m}}$ and $[\beta] = s^{-1}$. These transformations lead to the following dimensionless equations:

$$\begin{cases} \ddot{q} + \arctan q + \epsilon q = -n\dot{z} \\ \ddot{z} + \arctan z + \epsilon z = n\dot{q} \end{cases}, \quad (3)$$

where $n = \frac{N}{\sqrt{am}}$ and the notation $\frac{d}{d\tau} = \dot{\square}$ is used. Note that the impulse excitation on the host system is replaced with an equivalent initial velocity $\dot{q}(0)$. The relation to the dimensional initial condition is $\dot{q}(0) = \frac{\sqrt{am}}{\gamma} \frac{dx(0)}{dt}$ and $\frac{dx(0)}{dt}$ follows from the impulse load $F\delta(t)$ as $\frac{dx(0)}{dt} = \int \frac{F\delta(t)}{m} dt = \frac{F}{m}$. Remark that the coupling term n is the only parameter that can be tuned to control the host system. The focus of this work is investigating the influence of this control parameter n and offering insights into the tuning strategy.

3 Complexification-averaging method

To study this system, first the Complexification-Averaging (CxA) method [24] is applied to obtain the slow flow equations, as done by Quinn et al. in [25]. Next, the bifurcations that these equations exhibit are investigated and the corresponding behaviours are analysed using phase plots and impulsive orbits.

3.1 Complexification

The following transformations are performed.

$$\begin{cases} \rho_1 e^{j\omega\tau} = \dot{q} + j\omega q \\ \rho_2 e^{j\omega\tau} = \dot{z} + j\omega z \end{cases} \quad (4)$$

Here, j is the imaginary unit, with $j^2 = -1$, $\omega \in \mathbb{R}$ is constant and $\rho_{1,2} \in \mathbb{C}$. One can see that $\rho_{1,2}$ are measures for the amplitude of the velocity of respectively q and z . Here, we implicitly assume one dominant high frequency, ω , and amplitude and phase modulation, captured by $\rho_{1,2}$. The validity of this assumption is assessed in Section 3.4. From (4), one can find the following expressions for q, \dot{q} and \ddot{q} . Analogous expressions can be found for z, \dot{z} and \ddot{z} .

$$\begin{aligned} q &= \frac{1}{2j\omega}(\rho_1 e^{j\omega\tau} - \rho_1^* e^{-j\omega\tau}) & z &= \frac{1}{2j\omega}(\rho_2 e^{j\omega\tau} - \rho_2^* e^{-j\omega\tau}) \\ \dot{q} &= \frac{1}{2}(\rho_1 e^{j\omega\tau} + \rho_1^* e^{-j\omega\tau}) & \dot{z} &= \frac{1}{2}(\rho_2 e^{j\omega\tau} + \rho_2^* e^{-j\omega\tau}) \\ \ddot{q} &= \dot{\rho}_1 e^{j\omega\tau} + j\omega\rho_1 e^{j\omega\tau} - j\omega\frac{1}{2}(\rho_1 e^{j\omega\tau} + \rho_1^* e^{-j\omega\tau}) & \ddot{z} &= \dot{\rho}_2 e^{j\omega\tau} + j\omega\rho_2 e^{j\omega\tau} - j\omega\frac{1}{2}(\rho_2 e^{j\omega\tau} + \rho_2^* e^{-j\omega\tau}) \end{aligned} \quad (5)$$

where \square^* denotes the complex conjugate. After substituting these expressions into Eq. (3), one finds

$$\begin{cases} \dot{\rho}_1 e^{j\omega\tau} + \rho_1 e^{j\omega\tau} \left(\frac{j\omega}{2} + \frac{\epsilon}{2j\omega} \right) - \rho_1^* e^{-j\omega\tau} \left(\frac{j\omega}{2} + \frac{\epsilon}{2j\omega} \right) + \arctan \left[\frac{1}{2j\omega} (\rho_1 e^{j\omega\tau} - \rho_1^* e^{-j\omega\tau}) \right] \\ \quad = -\frac{n}{2} (\rho_2 e^{j\omega\tau} + \rho_2^* e^{-j\omega\tau}) \\ \dot{\rho}_2 e^{j\omega\tau} + \rho_2 e^{j\omega\tau} \left(\frac{j\omega}{2} + \frac{\epsilon}{2j\omega} \right) - \rho_2^* e^{-j\omega\tau} \left(\frac{j\omega}{2} + \frac{\epsilon}{2j\omega} \right) + \arctan \left[\frac{1}{2j\omega} (\rho_2 e^{j\omega\tau} - \rho_2^* e^{-j\omega\tau}) \right] \\ \quad = \frac{n}{2} (\rho_1 e^{j\omega\tau} + \rho_1^* e^{-j\omega\tau}) \end{cases} \quad (6)$$

3.2 Averaging

In order to analyse the slow time behaviour, Eq. (6) can be averaged over the fast period.

$$\frac{d\bar{\rho}_i}{d\tau} = \frac{\omega}{2\pi} \int_{\tau-\frac{\pi}{\omega}}^{\tau+\frac{\pi}{\omega}} \dot{\rho}_i(\tau) d\tau \quad (7)$$

The variables $\bar{\rho}_i$ ($i = 1, 2$) represent the running average of ρ_i over one period $\frac{2\pi}{\omega}$. Due to ρ_i being slowly varying, as assumed in the complexification step, the running averages $\bar{\rho}_i$ approximate ρ_i .

By applying Eq. (7), the following equations are obtained.

$$\begin{cases} \frac{d\bar{\rho}_1}{d\tau} = -\bar{\rho}_1 \left(\frac{j\omega}{2} + \frac{\epsilon}{2j\omega} \right) - \frac{n}{2} \bar{\rho}_2 + \frac{j\omega \bar{\rho}_1}{\bar{\rho}_1 \bar{\rho}_1^*} \left(\sqrt{\frac{\bar{\rho}_1 \bar{\rho}_1^*}{\omega^2} + 1} - 1 \right) \\ \frac{d\bar{\rho}_2}{d\tau} = -\bar{\rho}_2 \left(\frac{j\omega}{2} + \frac{\epsilon}{2j\omega} \right) + \frac{n}{2} \bar{\rho}_1 + \frac{j\omega \bar{\rho}_2}{\bar{\rho}_2 \bar{\rho}_2^*} \left(\sqrt{\frac{\bar{\rho}_2 \bar{\rho}_2^*}{\omega^2} + 1} - 1 \right) \end{cases} \quad (8)$$

The obtained averaged equations describe the slow flow behaviour: $\bar{\rho}_1$ and $\bar{\rho}_2$ are an approximation of the envelopes of the time responses of \dot{q} and \dot{z} , respectively, as illustrated in Fig. 3.

3.3 Transformation to polar coordinates

To interpret the slow flow equations, we are interested in the magnitude and phase of $\bar{\rho}_i$, $i = 1, 2$. Therefore, a transformation to polar coordinates is introduced:

$$\begin{cases} \bar{\rho}_1 = a_1 e^{j\theta_1} \\ \bar{\rho}_2 = a_2 e^{j\theta_2} \end{cases} \quad (9)$$

with, $a_{1,2} \in \mathbb{R}$ and $\theta_{1,2} \in \mathbb{R}$. Defining $\phi = \theta_1 - \theta_2$, one obtains a new set of equations governing the slow behaviour. Note that ϕ represents the phase difference between \dot{q} and \dot{z} , while a_1 and a_2 represent the amplitudes of the envelopes of \dot{q} and \dot{z} respectively.

$$\begin{cases} \dot{a}_1 = -\frac{n}{2} a_2 \cos(\phi) = f_1(a_1, a_2, \phi) \\ \dot{a}_2 = \frac{n}{2} a_1 \cos(\phi) = f_2(a_1, a_2, \phi) \\ \dot{\phi} = \frac{n}{2} \sin(\phi) \left(\frac{a_2}{a_1} - \frac{a_1}{a_2} \right) + \omega \left[\frac{\sqrt{\frac{a_1^2}{\omega^2} + 1} - 1}{a_1^2} - \frac{\sqrt{\frac{a_2^2}{\omega^2} + 1} - 1}{a_2^2} \right] = f_3(a_1, a_2, \phi) \end{cases} \quad (10)$$

Note that r is an integral of motion of this system.

$$\begin{aligned} r^2 &= a_1^2 + a_2^2 \\ 2r\dot{r} &= 2a_1\dot{a}_1 + 2a_2\dot{a}_2 = 0 \end{aligned} \tag{11}$$

Using this integral of motion, we can lower the dimension from a third-order to a second-order system of equations.

Furthermore, r is a measure for the energy in the controlled (conservative) system. As an impulsive load on the host system is considered, at $t = 0$ there is only kinetic energy, $E(0) = \frac{m}{2}\dot{x}(0)^2$. The relationship between the initial conditions is $r = a_1(0) = \dot{q}(0) = \frac{\sqrt{am}}{\gamma}\dot{x}(0)$. Thus, as a_1 is a measure for the envelope of \dot{q} and consequently proportional to \dot{x} , r^2 is also a measure for the energy in the system: $r^2 \propto a_1(0)^2 \propto \dot{q}(0)^2 \propto \dot{x}(0)^2 \propto E$.

3.4 Validity of slow flow equations

In Figure 3, the slow flow amplitudes a_1 and a_2 from Eq. (10) with initial conditions $a_1(0) = r$, $a_2(0) = 0$ are plotted together with the time responses of \dot{q} and \dot{z} from Eq. (3) with initial condition $\dot{q}(0) = r$. One can see that the slow flow amplitudes, a_1 and a_2 , are good measures for the envelopes of the time responses of \dot{q} and \dot{z} . For the cases here where $r = 0.5$ and/or $n = 0.2$ (Figs. 3a, 3d, 3g, 3h and 3i), we see a beating phenomenon. This means, at some point, the amplitude of a_1 is minimal while a_2 is maximal, and most energy has been transferred from the host system to the controller.

For a certain energy range ($r \leq 3$, see Fig. 3), the assumptions made during the complexification in Eq. (4) are valid. Although the periods of the envelopes obtained from the slow flow equations are not exact (for example, in Fig. 3e), they do capture the amplitudes of \dot{q} and \dot{z} well and they can accurately describe whether energy is exchanged between the host system and the controller.

However, for high energy, as depicted in Fig. 4 and most noticeable in 4c, the slow flow equations fail to capture the behaviour of the system. The responses of \dot{q} and \dot{z} resemble a sawtooth wave, which indicates the presence of third and higher-order harmonics. Therefore, the assumptions made with respect to the dominant frequencies lose their validity. Furthermore, for some values of n and $r > 3$ the system seems to exhibit chaotic behaviour. This is investigated further in Section 3.4.1.

3.4.1 Chaotic nature of system

According to S. H. Strogatz, chaos can be defined by three key behaviours [28]: aperiodic long-term behaviour, being deterministic, and sensitive dependence on initial conditions.

For high enough energies, chaos-like behaviour can be observed. To support this statement, Figure 5 shows aperiodic long-term behaviour. Next, the system is described by Equation (2) or (3) and is by definition deterministic. Finally, by showing two very close initial conditions with very different responses, the third condition is fulfilled. A closer look at the responses between 1000-1250s on Fig. 5 shows clearly

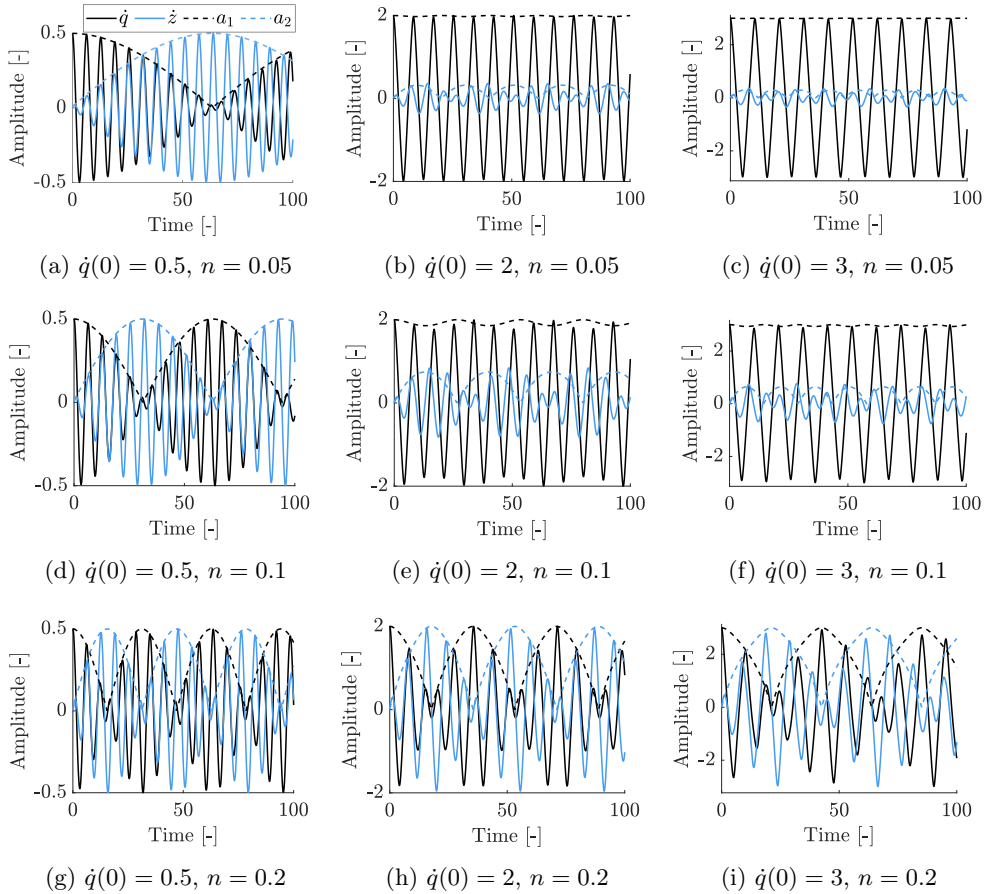


Fig. 3: Time responses and slow flow behaviour for different energies and values of n .

different behaviour for a slightly higher impulse load. Moreover, a positive maximal Lyapunov exponent confirms this condition of sensitive dependence on initial conditions.

The method by R. Wiebe et al. [29] offers a strategy for identifying chaos based on the frequency content. The method is based on the phenomenon that the frequency spectrum of a chaotic response has more peaks than a well-behaved response. First, the frequency spectrum of the response of the host system is obtained and scaled such that the highest peak has a magnitude of one. Next, a threshold is chosen, usually a small percentage of the maximal peak height. Here, this threshold is set to 0.05 or 5% of the maximal peak value. Finally, the number of peaks that rise above the threshold is counted. This metric is visualised in Fig. 6 for a range of $r = [0, 5]$ and $n = [0, 0.3]$. The blue (darker) areas have few peaks in their frequency spectrum, the cases that are green and yellow (lighter areas) have more. One can remark the area with more frequency peaks around $n = 0.2$ and $r \in [3, 5]$.

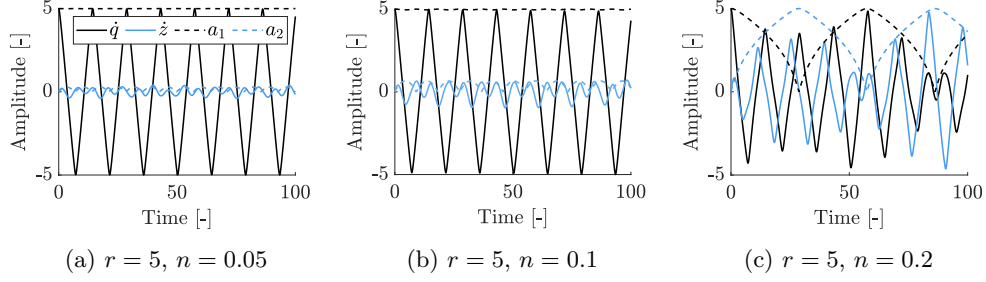


Fig. 4: Time responses and slow flow behaviour for high energy and different values of n .

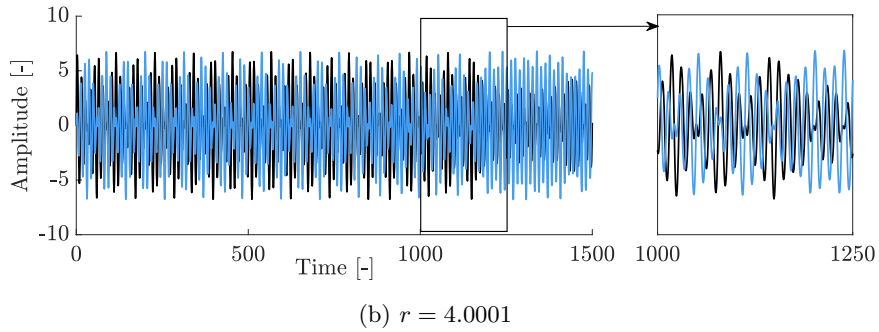
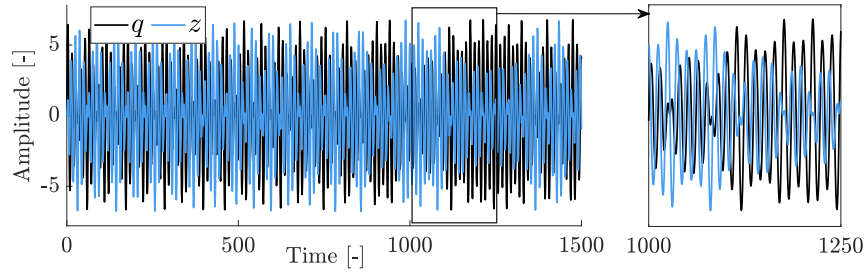


Fig. 5: Time responses of q and z for $n = 0.2$ with slightly different initial conditions

Finally, a second threshold is chosen to discern well-behaved and chaotic responses. Responses with a peak count of ten or more are classified as chaotic, and visualised in Figure 7. Notably, these chaotic responses can occur for $r > 3$.

To substantiate this result, time responses and frequency spectra are shown in Fig. 8 for the four cases indicated with A, B, C and D on Fig. 6. Case C is in the chaotic region. Its frequency spectrum in Fig. 8f is distinctively different from the other cases and clearly shows how chaos manifests itself in the frequency response.

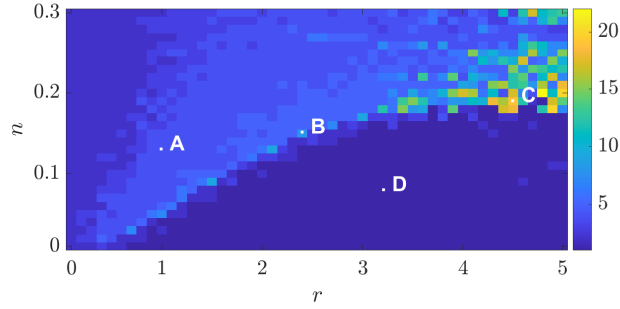


Fig. 6: Number of local maxima of the frequency spectrum above the threshold

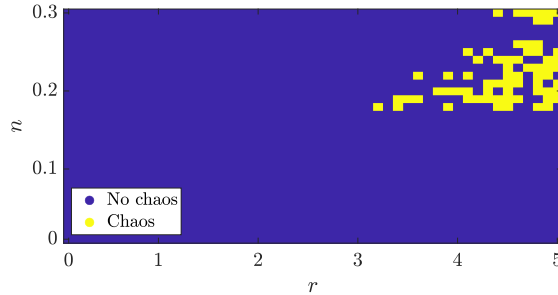


Fig. 7: Classification of chaos according to [29] using a threshold of 10 peaks

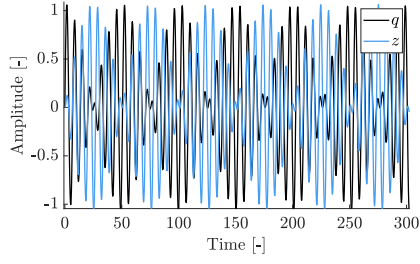
As chaotic behaviour requires a different control approach, the energy range is limited in this analysis. Values for r are considered up to 3 to avoid the chaotic region and ensure the assumptions remain relevant. This limit on the dimensionless parameter $r \leq 3$ means that the dimensionless initial velocity of the host system is limited to $\dot{q}(0) \leq 3$ and the physical velocity is limited to $\dot{x}(0) \leq \frac{3\gamma}{\sqrt{am}}$. This way, in the regarded energy range, the slow flow equations can lead to valuable insights into the influence of n on the energy exchange between the host system and the VMS controller.

4 Bifurcation analysis

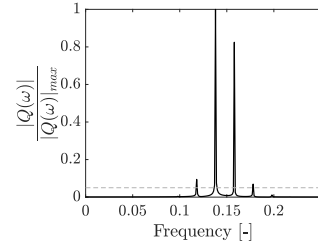
Bifurcation analysis is a method that offers a comprehensive understanding of the system's dynamics. A local bifurcation occurs when a parameter variation causes a qualitative change in dynamics. For example, fixed points can be created, destroyed or change its stability [28]. In order to find a threshold for energy transfer from the host to the controller, the fixed points are investigated.

4.1 Fixed points

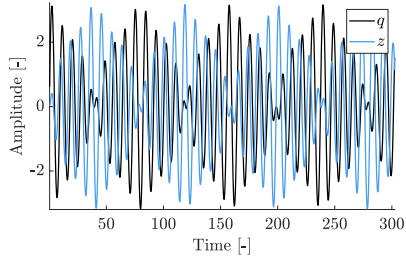
Fixed points represent equilibrium or steady state solutions of a system. To find the fixed points of the slow flow equations, we set $f_1(a_1, a_2, \phi) = 0$, $f_2(a_1, a_2, \phi) = 0$ and



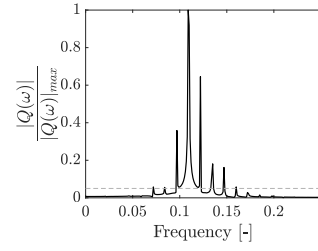
(a) A: $n = 0.13$, $r = 1$



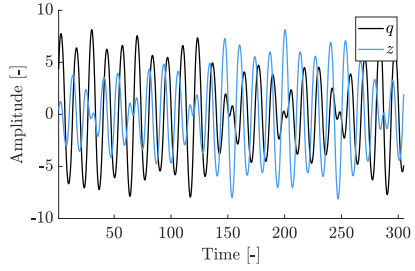
(b) A: $n = 0.13$, $r = 1$



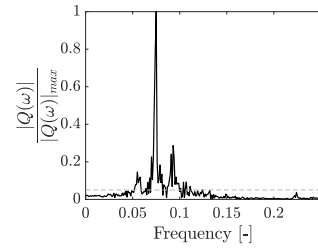
(c) B: $n = 0.15$, $r = 2.4$



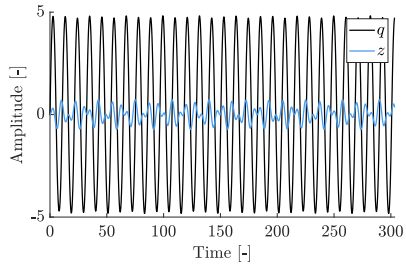
(d) B: $n = 0.15$, $r = 2.4$



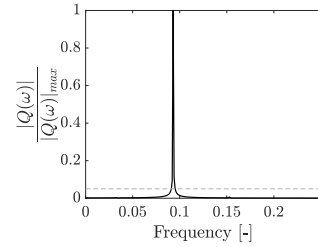
(e) C: $n = 0.18$, $r = 3.4$



(f) C: $n = 0.18$, $r = 3.4$



(g) D: $n = 0.08$, $r = 3.2$



(h) D: $n = 0.08$, $r = 3.2$

Fig. 8: Time responses and frequency spectra for cases shown in Fig. 6

$f_3(a_1, a_2, \phi) = 0$, where $f_{1,2,3}$ are defined in Eq. (10). Analytically, from the first two equations, we can conclude that $\phi = \pm\frac{\pi}{2}$ is required to guarantee that f_1 and f_2 are zero. The only other solution is $a_1 = a_2 = 0$, corresponding to the system at rest. To find the fixed points, $f_3 = 0$ must be solved for both values of ϕ . This is investigated in the next paragraphs.

4.1.1 Case 1: $\phi = \frac{\pi}{2}$

To find the expressions of the fixed points, the third equation from Eq. (10) must be solved for $\phi = \frac{\pi}{2}$.

$$\dot{\phi}\Big|_{\phi=\frac{\pi}{2}} = \frac{n}{2} \left(\frac{a_2}{a_1} - \frac{a_1}{a_2} \right) + \omega \left[\frac{\sqrt{\frac{a_1^2}{\omega^2} + 1} - 1}{a_1^2} - \frac{\sqrt{\frac{a_2^2}{\omega^2} + 1} - 1}{a_2^2} \right] = 0 \quad (12)$$

This equation is evaluated numerically for different values of n and r , defined by Eq. (11). The results are plotted in Fig. 9 as a function of a_1 . Note that, as r is fixed, a_2 is completely defined by a_1 . The behaviour for $n \in [10^{-5} 1]$ and $r \in [10^{-5} 3]$ is qualitatively the same.

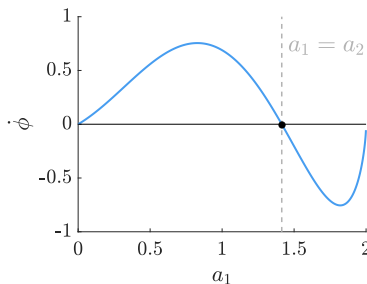


Fig. 9: $\dot{\phi}\Big|_{\phi=\frac{\pi}{2}}$ in function of a_1 , here $r = 2$, $n = 0.2$

Expression (12) only becomes zero if $a_1 = a_2$, the outer points of the graph correspond to $a_1 = 0$ and $a_1 = r$, equivalent to $a_2 = 0$. In these two cases, expression (12) is undefined. The only solution here, considering $a_1 a_2 > 0$, is $a_1 = a_2$. This solution corresponds to a line of fixed points in the space (a_1, a_2, ϕ) , depicted in Fig. 10. However, when regarding a constant energy level, or equivalently a fixed r , this line of fixed points becomes an isolated point on the half sphere of constant r . Note that we only regard a_1 and a_2 having the same sign, as having different signs is equivalent to a phase shift of π rad, i.e. the case where $\phi = -\frac{\pi}{2}$, investigated in Section 4.1.2.

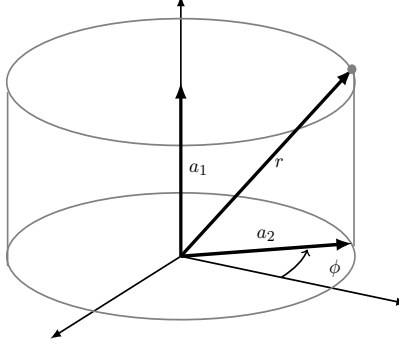


Fig. 10: Coordinate reference frame for slow flow equations

Stability of fixed points

The stability of these fixed points is investigated using the Jacobian.

$$J \Big|_{\phi=\frac{\pi}{2}; a_1=a_2=a} = \begin{bmatrix} 0 & 0 & \frac{na}{2} \\ 0 & 0 & -\frac{na}{2} \\ J_{31} & -J_{31} & 0 \end{bmatrix} \quad (13)$$

Here $a = \frac{r}{\sqrt{2}} \in \mathbb{R}$, and

$$J_{31} = -\frac{n}{a} + \omega \left[\frac{-\frac{a^2}{\omega^2} + 2\sqrt{\frac{a^2}{\omega^2} + 1} - 2}{a^3 \sqrt{\frac{a^2}{\omega^2} + 1}} \right]. \quad (14)$$

The eigenvalues of the Jacobian in this case are $\lambda_1 = 0$ and $\lambda_{2,3} = \pm \sqrt{naJ_{31}}$. As we have a line of fixed points, the zero eigenvalue is expected. To find out what type of fixed points we are dealing with, the sign of naJ_{31} is of importance.

$$aJ_{31} = n + \omega \left[\frac{\frac{a^2}{\omega^2} + 2\sqrt{\frac{a^2}{\omega^2} + 1} - 2}{a^2 \sqrt{\frac{a^2}{\omega^2} + 1}} \right] \quad (15)$$

This expression is evaluated numerically for $n \in [10^{-5} 1]$ and $r \in [10^{-5} 3]$. A numerical investigation shows that this factor is always negative. This means, considering the system is reversible (see Section 4.2), that the fixed points are nonlinear centres on each surface of constant energy.

4.1.2 Case 2: $\phi = -\frac{\pi}{2}$

The expression for $\dot{\phi}$, given that $\phi = -\frac{\pi}{2}$ becomes

$$\dot{\phi} \Big|_{\phi=\frac{\pi}{2}} = -\frac{n}{2} \left(\frac{a_2}{a_1} - \frac{a_1}{a_2} \right) + \omega \left[\frac{\sqrt{\frac{a_1^2}{\omega^2} + 1} - 1}{a_1^2} - \frac{\sqrt{\frac{a_2^2}{\omega^2} + 1} - 1}{a_2^2} \right] = 0 \quad (16)$$

As in Section 4.1.1, $a_1 = a_2$ remains a solution for every n . However, in this case, there are more fixed points possible. The extra fixed points are numerically investigated for fixed r and n .

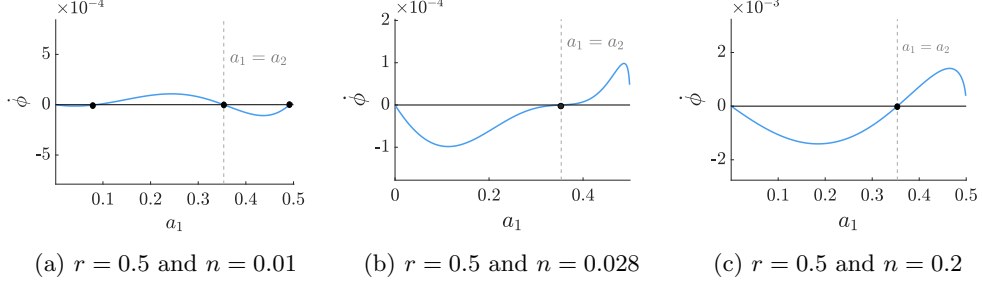


Fig. 11: $\dot{\phi} \Big|_{\phi=-\frac{\pi}{2}}$ in function of a_1 for $r = 0.5$ and different values of n

In Fig. 11, the course of $\dot{\phi} \Big|_{\phi=-\frac{\pi}{2}}$ (Eq. 16) is plotted in function of a_1 , while r is fixed to be $r = 0.5$. The zeros of this expression are indicated with black dots and represent fixed points of the slow flow dynamics. For small n , there are three fixed points: one at $a_1 = a_2 = \frac{r}{\sqrt{2}}$ and two outer points very close to $a_1 = 0$ and $a_1 = r$. For increasing n , the outer points get closer to $a_1 = a_2$ and around $n = 0.028$, these two fixed points disappear, so only the fixed point at $a_1 = a_2$ remains. The same behaviour can be seen for a higher energy level.

To clarify the relationship between n , r and the number of fixed points, Fig. 12 shows the fixed points in the $(a_1, a_2, \phi = -\frac{\pi}{2})$ plane for different values of n . The distance to the origin is r . Remember that r is a measure for the energy in the system. The figure is created by numerically evaluating Eq. (16) for fixed n and r to find the values of a_1 and a_2 of the fixed points.

As shown in Fig. 12, the fixed points at $a_1 = a_2$ are present for all n , while the curved line of fixed points varies with n . Looking at the case where $n = 0.2$, we see that if $r = 1$, there is only 1 intersection between the dashed arc of constant r and the black lines of fixed points for $n = 0.2$. The only fixed point in this case is $a_1 = a_2 = \frac{1}{\sqrt{2}}$. When we increase r to 1.383, the dashed arc touches the location where two extra fixed points appear. A red circle on the figure indicates this case. For $n = 0.2$, the bifurcation takes place at $r = 1.838$. For lower energy levels (ex. $r = 1$), there is one fixed point and for higher energy levels (ex. $r = 3$) there are three fixed points. The higher n , the higher the energy at which the bifurcation occurs.

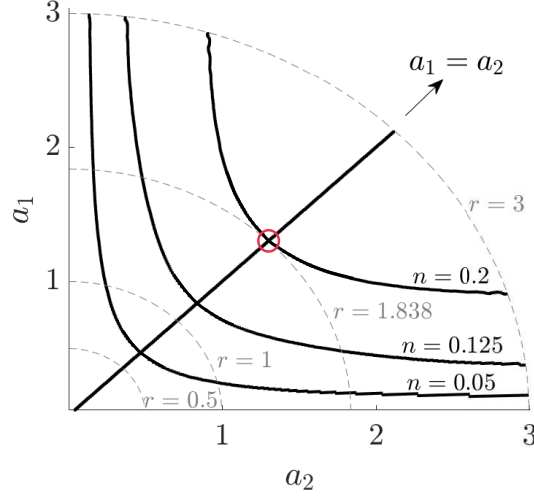


Fig. 12: Fixed points for $\phi = -\frac{\pi}{2}$ for different values of n

From a control perspective, as n is the tuning parameter and r depends on the magnitude of the impulse, it is more interesting to consider a fixed r and look at the influence of a varying n . Considering $r = 1.838$, choosing $n > 0.2$ results in only one fixed point, while choosing $n < 0.2$ leads to three fixed points. Furthermore, the smaller n , the closer the two extra fixed points are to the axes ($a_1 = 0$ and $a_2 = 0$).

Do note that, in this section, only the fixed points for $\phi = -\frac{\pi}{2}$ are regarded. There is always one supplementary fixed point for $\phi = \frac{\pi}{2}$ present, independent of the values of r and n . In general, for a fixed n , small energy levels correspond to two fixed points at $a_1 = a_2$ and $\phi = \pm\frac{\pi}{2}$. When r increases, a bifurcation occurs and two extra fixed points appear, leading to four fixed points in total.

Stability of fixed points

For the fixed point at $a_1 = a_2$, the Jacobian can be evaluated to find its type.

$$J \Big|_{\phi = -\frac{\pi}{2}; a_1 = a_2 = a} = \begin{bmatrix} 0 & 0 & -\frac{na}{2} \\ 0 & 0 & \frac{na}{2} \\ K_{31} & -K_{31} & 0 \end{bmatrix} \quad (17)$$

Where

$$K_{31} = \frac{n}{a} + \omega \left[\frac{\frac{a^2}{\omega^2} - 2\sqrt{\frac{a^2}{\omega^2} + 1} + 2}{a^3\sqrt{\frac{a^2}{\omega^2} + 1}} \right]. \quad (18)$$

The eigenvalues of the Jacobian are calculated to be $\lambda_1 = 0$ and $\lambda_{2,3} = \pm\sqrt{-naK_{31}}$.

A numerical evaluation for fixed n shows that, for the low energy region, where there is only 1 fixed point, $\lambda_{2,3}$ are imaginary, and thus, the fixed point is a centre

on the surface of constant energy. When the energy is increased, $\lambda_{2,3}$ become 2 real roots with opposite sign. The instance when $\lambda_{2,3}$ become real is when the bifurcation occurs and two extra fixed points appear. After this bifurcation, the fixed point at $a_1 = a_2 = \frac{r}{\sqrt{2}}$ becomes a saddle point on the surface of constant energy and the two new fixed points are nonlinear centres.

4.2 Reversibility

The undamped system in Eq. (3) is reversible under the transformation

$$\begin{cases} (q, z) \mapsto R(q, z), & \text{where } R(q, z) = (-q, -z) \\ t \mapsto -t. \end{cases} \quad (19)$$

This property allows us to make conclusions about nonlinear centres based on the Jacobian.

4.3 Phase plots

The dynamics of the slow flow equations can be visualised in a 3D plot. Figure 10 shows the chosen reference frame. Recall that $r^2 = a_1^2 + a_2^2$ is an integral of motion, as shown in Eq. (11). This means the trajectories of the slow flow dynamics are bounded to a spherical surface in the (a_1, a_2, ϕ) space with a centre at the origin and radius $r = \sqrt{a_1^2 + a_2^2}$, corresponding to the energy of the system.

Further, as a_1 represents an amplitude modulation, a negative sign does not add any new information. Thus, we can consider only the top half section of the sphere without loss of information. And consequently, depict the trajectories in a 2D graph by regarding the top view (from the a_1 direction in Fig. 10). This top view of the trajectories on the sphere for $r = 1$ is shown in Figure 13b. Note that the blue line corresponds to $\phi = \frac{\pi}{2}$, and there is one fixed point (centre) on this line at $a_1 = a_2 = \frac{r}{\sqrt{2}}$. The red line corresponds to $\phi = -\frac{\pi}{2}$ and can have one or three fixed points. For the case depicted in Fig. 13b, $r = 1$ and $n = 0.05$, leading to three fixed points, one centre and two saddle points. Figure 13a can be seen as a cross section of Figure 13b at $\phi = -\frac{\pi}{2}$ (indicated by the red line). The fixed points indicated in red on Fig. 13a are the ones visible on the phase plot in Fig. 13b.

This way of representing the phase plots leads to the origin corresponding to a_1 being maximal ($a_1 = r$ and $a_2 = 0$), so all energy is in the host system. On the circumference of this view, $a_2 = r$, $a_1 = 0$ and all energy is in the controller. This means that the behaviour we are looking for corresponds to a trajectory which starts in the origin (all energy is situated in the host system initially because of the applied initial speed) and goes to the outer area of the plot, which corresponds to all energy being in the controller. The control parameter n should be chosen in a way to ensure this energy transfer.

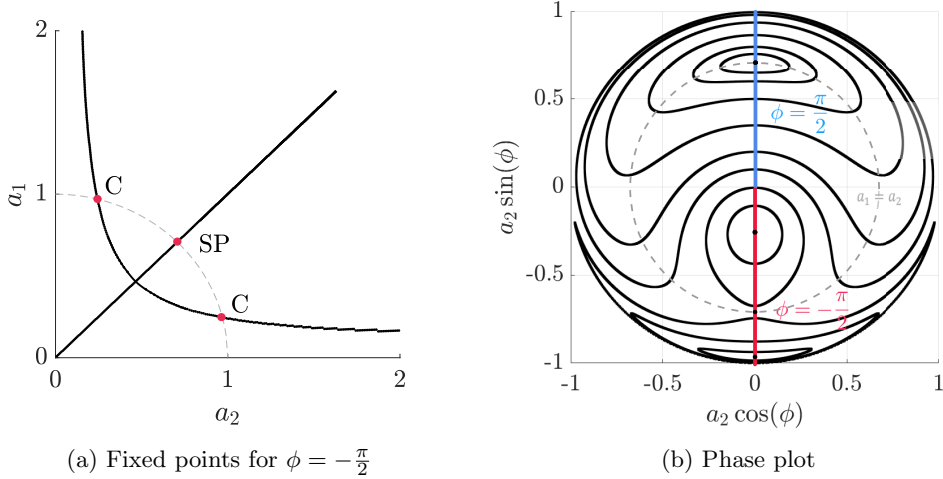


Fig. 13: Fixed points and phase plot for $r = 1$ and $n = 0.05$

4.4 Impulsive orbits

An impulsive orbit is the trajectory of the slow flow dynamics, described by Eq. (10), followed if an impulse is applied to one of the degrees of freedom. Here, we consider the case where an impulse is exerted on the host system, equivalent to the initial conditions $a_1(0) = r > 0$ and $a_2(0) = 0$. Some impulsive orbits are depicted in red on the phase plots in Fig. 14. The starting point is the origin of the plots, indicated with a square marker. The course of the impulsive orbit corresponds to the location of the energy within the controlled system. If it stays close to the origin, the energy remains mostly in the host system. If it reaches the outer area on the other hand, a_2 approaches r and we can conclude energy transfer to the controller is significant.

5 Results and discussion

An analysis of the phase plots and impulsive orbits can clarify the behaviour of the system. They are shown for the case of $r = 1$ in Figure 14. The lines are trajectories of the slow flow dynamics. Indicated in red are the impulsive orbits, which start in the origin indicated with a square marker, and in blue are the homoclinic orbits, which end at the saddle point.

The time responses corresponding to the impulsive orbits are depicted in 15. In Fig. 15a, the energy stays mostly in the host system. After the impulsive orbit escapes the homoclinic orbit, energy transfer occurs, as seen in Fig. 15b. Do note that the energy transfer here is relatively slow (see time axis). This is due to the trajectory being close to the saddle point, which slows down the dynamics. This also means that around the energy transfer threshold, the assumption of a fast frequency ω and slow amplitude modulation captured in ρ_i is always valid. For n increased further, two fixed points

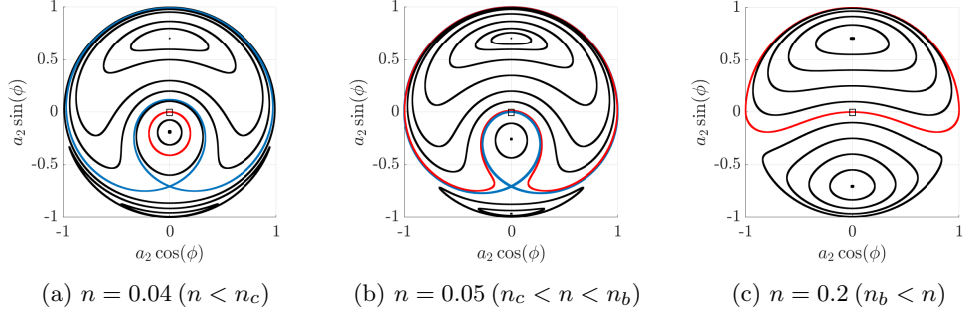


Fig. 14: Phase plots for $r = 1$ and different values of n with impulsive orbits indicated in red and homoclinic orbits in blue

disappear. The time response in Fig. 15c show that the energy transfer is maintained and the amplitude modulation varies faster.

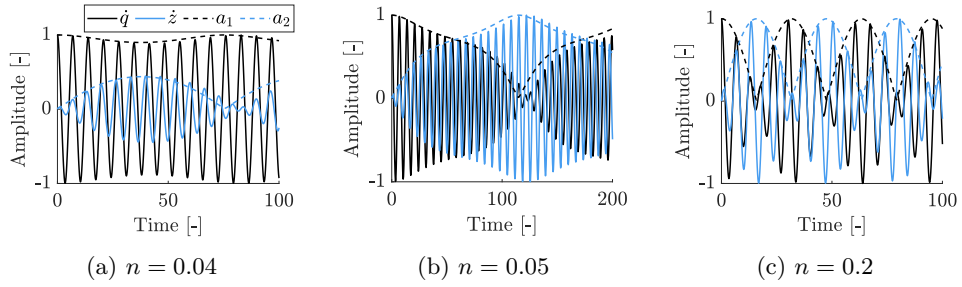


Fig. 15: Time responses corresponding to the impulsive orbits indicated on the phase plots in Fig. 14 for $r = 1$ and different values of n

As the control parameter n increases, the first change in fundamental behaviour is induced by the impulsive orbit escaping the homoclinic orbit, at a critical value n_c . The next one is the bifurcation at n_b , where the transition from four fixed points to two fixed points occurs. The cases $n < n_c$, $n_c < n < n_b$ and $n_b < n$ are discussed in-depth in the next sections.

5.1 $n < n_c$

For small values of n , as shown in Figure 14a, there are four fixed points. One fixed point for $\phi = \frac{\pi}{2}$ and three for $\phi = -\frac{\pi}{2}$. The two centres for $\phi = -\frac{\pi}{2}$ are situated close to $a_1 = r$, $a_2 = 0$ (the origin) and $a_1 = 0$, $a_2 = r$ (the bottom of the plot). This can be confirmed by looking at Fig. 12. The smaller n , the closer two of the fixed points are to the axes. Note that the saddle point always remains located at $a_1 = a_2 = \frac{r}{\sqrt{2}}$.

Due to this placement of the centres, the homoclinic orbit, which ends in the saddle point, traps the impulsive orbit. Therefore, the impulsive orbit stays close to the origin and most energy remains in the host system. This is also illustrated in Fig. 15a.

5.2 $n_c < n < n_b$

As n increases, the two centres for $\phi = -\frac{\pi}{2}$ move closer to the saddle point, see Fig. 12. For a critical value of $n = n_c$, the homoclinic orbit coincides with the impulsive orbit and the trajectory starting in the origin ($a_1 = r$, $a_2 = 0$) ends in the saddle point for $\tau \rightarrow \infty$.

Once $n > n_c$, the impulsive orbit escapes the homoclinic orbit and reaches the area where $a_2 \approx r$. This means approximately all energy is transferred from the host system to the controller. Do note that this transfer of energy is relatively slow when the impulsive orbit is close to the saddle point, as Fig. 15b shows.

5.3 $n > n_b$

By increasing the control parameter n even further, a bifurcation occurs and only two fixed points remain, which are both centres. In this case, the impulsive orbit always reaches the outer area, see Fig. 14c, and energy is transferred consistently between the host system and the VMS controller through nonlinear beating, which is visible on the time response in Fig. 15c.

5.4 Bifurcation diagram

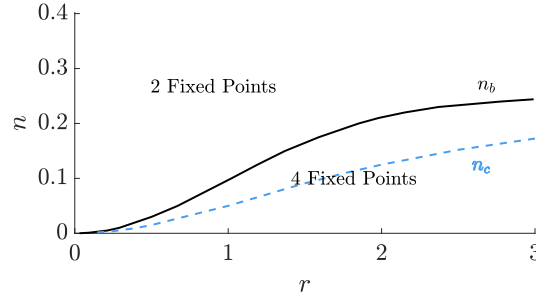


Fig. 16: Bifurcation diagram, with energy transfer threshold value n_c indicated in a dashed blue line

These insights can be generalised to other values of r using the bifurcation diagram in Figure 16. This diagram is achieved by evaluating n_b and n_c for a range $r \in [0, 3]$. Here, n_b is calculated by evaluating how many fixed points are present according to Eq. (16), as explained in Section 4.1.2. While n_c is calculated by evaluating the slow flow equations (10). More specifically, when a_1 goes to zero, energy transfer is present.

Once again, three areas can be considered in this bifurcation diagram. The thick black line represents n_b , where the bifurcation occurs. This line separates the situations where two or four fixed points are present. The dashed line represents n_c , the critical threshold for energy transfer. The area under the dashed line on the diagram corresponds to most energy remaining in the host system. Above the dashed line, significant energy transfer to the controller is achieved. The larger the control parameter n , corresponding to higher areas on the diagram (for a fixed r), the faster the energy flows back and forth between the host system and the controller. Using this diagram, the threshold for energy transfer n_c can be found for any value of r within the regarded range.

Remark that the dashed line of n_c on Fig. 16 corresponds to the visible border of Fig. 6. Under this line, there are fewer frequency peaks and no energy transfer. For the cases where significant energy transfer to the controller is present, the response contains more frequencies.

5.5 Discussion on controller tuning

Figure 16 gives an understanding of which values of the control parameter n lead to energy transfer between host and controller and which values do not. Recall that the skew-symmetric appearance of n in the equations of motion creates an energy-conserving interconnection. As in gyroscopic systems, this type of connection creates a 90° phase shift, which induces energy transfer between the coupled systems. The goal is, first, to transfer the energy to the controller system. Second, the energy is inhibited from travelling back to the host by harvesting or dissipation. A good choice for n depends on set control objectives and practical considerations. Here, two general trade-offs are discussed.

5.5.1 Speed of energy transfer

To make a well-founded choice for n , one must take into consideration the speed of energy transfer. The trajectories near the homoclinic orbit are very slow, so choosing n near the dashed line on Fig. 16 will lead to slower changes in a_1 , a_2 and ϕ and consequently, slower energy transfer. For a certain energy level (a fixed r), the higher n , the faster the amplitude modulation and energy transfer. Although it might seem that choosing n very large is a good solution when attempting to induce energy transfer to the controller, do note that the higher n , the faster energy is also transferred back. Depending on the energy dissipation strategy, n will have a maximal useful value. A higher n and faster energy transfer will make it difficult to avoid energy being transferred back to the host system.

5.5.2 Beat quality

An example of an energy dissipation strategy is found in [9] and [30], where controller damping is switched on when all the energy is in the controller and thus energy transfer back to the host system is avoided. To be able to implement this, the timing is important. One must be able to track the envelope of the time signals online to estimate the instant when the envelope of the response of the host system is minimal, meaning

the vibration energy is mostly in the controller and damping should be switched on. A higher beat quality makes the envelope tracking more straightforward. Therefore, there is another trade-off, which relates to the beat quality BQ .

Beat quality can be defined as follows [30].

$$BQ = \frac{T_{env}}{T_{carr}} \quad (20)$$

Here, T_{env} is the period of the modulation of the response, or twice the period of a_1 or a_2 . $T_{carr} = \frac{2\pi}{\omega}$ is the carrier period, or the period of the fast oscillations. Low and high beat quality is illustrated in Fig. 17. In Fig. 17a, the beat quality is two, which intuitively is not an advantageous situation. The beat phenomenon cannot be noticed and it is hard to speak of energy moving to and from the controller. In Fig. 17b however, there is a clear beat phenomenon. If the host shows this response, there is clear energy transfer to the controller and back. The ideal beat quality depends on the specific control objective. It is clear in any case that beat quality must be taken into account when tuning the control parameter n .

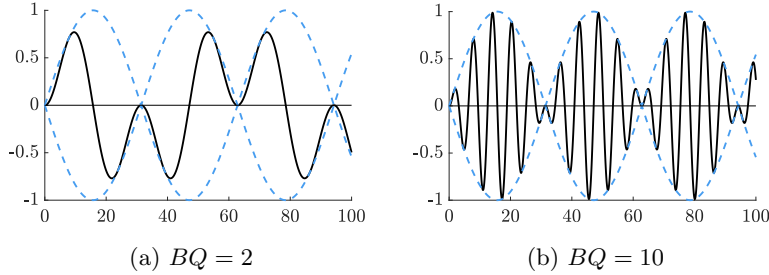


Fig. 17: Illustration of beat quality, with time signals in black and amplitude modulation in a blue dashed line

The beat quality is also a measure of how easily one can detect the moment at which the energy flow between the host system and controller reverses direction. Tracking the amplitude modulation online requires a certain amount of information and becomes easier the higher the beat quality is. This tracking can be important, depending on the applied energy dissipation strategy.

To illustrate the relationship between the beat quality and n , the values of BQ are depicted for different values for r and n on the bifurcation diagram in Fig. 18. The beat quality is only defined if energy is exchanged, corresponding to the area above the dashed line on the figure. For a specific r , the higher n , the lower the beat quality. The cases where $BQ = 10$, are indicated with a light grey line. The cases for low n ($n \gtrsim n_c$) and r have a very high beat quality. This is due to the very slow envelope dynamics for trajectories near the saddle point. Note that for $n \leq 0.02$ and $r < 0.5$, BQ is higher than 80 and not captured by the scale shown. However, the exact values are not important, as these cases are not interesting from a control perspective.

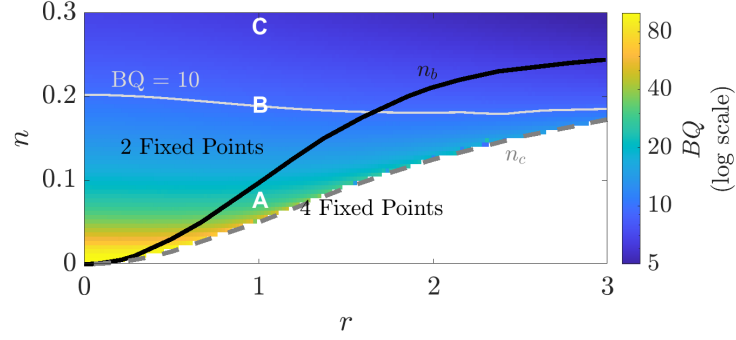


Fig. 18: Bifurcation diagram, with energy transfer threshold value n_c indicated in a dashed blue line and beat quality indicated in colour

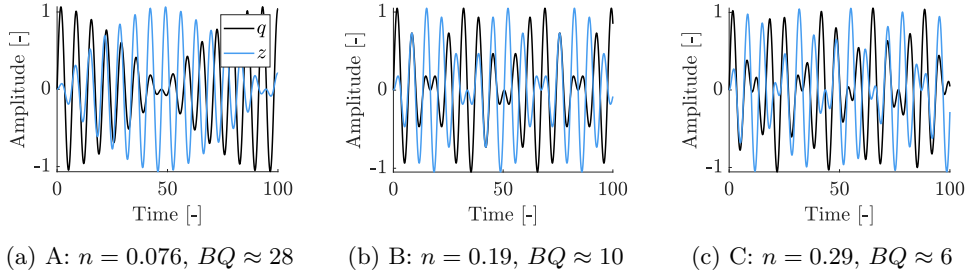


Fig. 19: Time responses for cases A, B and C shown in Fig. 18 for $r = 1$ and different values of n

Considering the envelope reconstruction and energy dissipation strategies, this plot can offer insight into the controller tuning to ensure useful energy transfer.

To illustrate this, three cases are indicated on Fig. 18 with A, B and C. The cases correspond to $r = 1$ and $n = 0.076$, 0.19 and 0.29 , respectively. The time responses for these cases are shown in Fig. 19. In case A, Fig. 19a, the envelope modulation is slow. It takes about 50s for the energy to transfer to the controller. However, the beat quality is very high, facilitating online envelope tracking. In case of B, Fig. 19b, it takes approximately one-third of the time to complete the energy transfer to the controller. Here, the beat quality is approximately 10. In case C, the energy is transferred the fastest, however, beat quality is low (approximately 6). This could cause difficulty in detecting the moment at which the energy flow reverses direction in real-time. A lower value for n , leads to a higher beat quality.

5.5.3 Practical considerations

First, robustness is considered from the point of view of parameter variations within the arctangent stiffness model $K(x) = \gamma \arctan \frac{a}{\gamma} x + \epsilon ax$. Further, model mismatch is discussed, where the softening stiffness law deviates from the arctangent expression.

Simulations have been done to observe the effect of parameter variation in the nonlinear stiffness of the host system. The slope a of the host system's stiffness is scaled by f , while the controller remains unchanged. Figures 20a and 20c show time responses for host systems with decreased and increased stiffness parameter a , respectively. Compared to the original case in Fig. 20b, one can note that there is still considerable energy transfer, but the envelope of the amplitude of q no longer goes to zero.

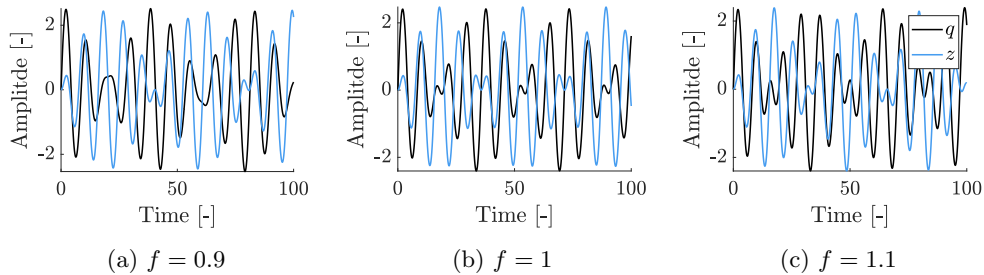


Fig. 20: Time responses for systems with imperfect parameter estimation of stiffness characteristic of host system, for $\dot{q}(0) = 2$ and $n = 0.2$

Regarding model mismatch, the case study in Section 6 will show that the proposed controller can also handle a different softening stiffness characteristic. However, further investigation is needed to determine to what extent the stiffness characteristic can differ from the proposed one, while remaining efficient.

6 Numerical example

The goal of this section is to illustrate the potential of the VMS control strategy using a numerical example. First, the insights into the control parameter n are implemented to induce energy transfer between the host and the controller systems. Afterwards, to prevent energy from flowing back to the host, a strategic damping term is added to the controller dynamics, effectively mitigating the vibrations.

6.1 Problem statement

The case study is based on the setup in [31]. The host is a compliant robotic end-effector, modelled as a mass-spring-damper system with softening stiffness. The equations of motion of the controlled system are given by Eq. (2), with parameters $m = 0.125\text{kg}$, $\gamma = 1\text{N}$, $a = 80\frac{\text{N}}{\text{m}}$ and $\epsilon = 10^{-2}$. The initial velocity, caused by a collision, is $\frac{dx}{dt}(0) = 0.6\frac{\text{m}}{\text{s}}$.

6.2 Tuning of control parameter n

To be able to use the dimensionless analysis, the dimensionless initial condition is calculated $\dot{q}(0) = \frac{\sqrt{am}}{\gamma} \dot{x}(0) = 1.8974 = r$. Knowing the expected value of r , the bifurcation diagram of Fig. 18 is used to tune n . The relevant parameters, r , n_c and n_b , for the considered initial condition are indicated in Fig. 21 and their numerical values are $r^* = 1.8974$, $n_c^* = 0.118$ and $n_b^* = 0.205$.

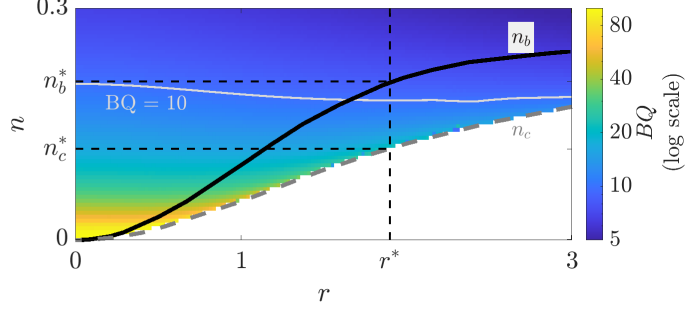


Fig. 21: Bifurcation diagram with relevant parameters for controller tuning

The two trade-offs that have been discussed are speed of energy transfer and beat quality. By choosing $n = n_c^*$, the highest BQ is achieved, while still ensuring energy transfer. However, if the initial impulse is a little higher ($r > r^*$), energy transfer does no longer occur for this choice of n and the speed of energy transfer is very slow for trajectories near the saddle point.

The trade-off is clear; the higher n , the lower the beat quality, but the faster energy is transferred to the controller. For these reasons, a value of $n = 0.18$ is chosen, corresponding to $BQ \approx 10$.

These values of the nondimensional system correspond to following control law with control force F_c :

$$\begin{cases} F_c = -N \frac{dy}{dt} \\ m \frac{d^2y}{dt^2} + \gamma \arctan \frac{a}{\gamma} y + \epsilon ay = N \frac{dx}{dt} \end{cases} \quad (21)$$

where the controller parameters are given by

$$\begin{aligned} m &= 0.125 \text{ kg} \\ \gamma &= 1 \text{ N} \\ a &= 80 \frac{\text{N}}{\text{m}} \\ \epsilon &= 0.01 \frac{\text{N}}{\text{m}} \\ N &= \sqrt{am} n = 0.5692 \frac{\text{Ns}}{\text{m}} \end{aligned} \quad (22)$$

This choice for n , leads to the behaviour in Fig. 23a.

6.3 Dissipation strategy

Having achieved this energy transfer and beat quality, the next step is to dissipate the energy before it is sent back to the host system. The authors acknowledge that an in-depth investigation is required and a simple example is given merely to illustrate the possibilities.

Damping is added to the controller dynamics.

$$\begin{cases} m \frac{d^2x}{dt^2} + \gamma \arctan \frac{a}{\gamma} x + \epsilon ax = -N \frac{dy}{dt} + \delta F \\ m \frac{d^2y}{dt^2} + C(x, \dot{x}) \frac{dy}{dt} + \gamma \arctan \frac{a}{\gamma} y + \epsilon ay = N \frac{dx}{dt} \end{cases}, \quad (23)$$

A conceptual characteristic for the damping factor is proposed, as shown in Figure 22. The damping factor $C(x, \dot{x})$ is chosen as a function of the energy in the host system E_h .

$$\begin{aligned} C(x, \dot{x}) &= \frac{C_{max}}{1 + e^{d(E_h(x, \dot{x}) - b)}} \\ E_h(x, \dot{x}) &= \frac{m}{2} \dot{x}^2 + \gamma \left(x \arctan \left(\frac{ax}{\gamma} \right) - \gamma \frac{\log(a^2 x^2 + \gamma^2)}{2a} \right) + \frac{\epsilon ax^2}{2} \end{aligned} \quad (24)$$

The parameters are chosen as follows $C_{max} = 2.2768$, $d = 5 \cdot 10^3$ en $b = 2.025 \cdot 10^{-3}$. When most energy is in the host system, low damping allows for energy to flow towards the virtual system, while when the host's energy is low, the damping factor is high and dissipates energy. As such the energy flow back to the host system is inhibited.

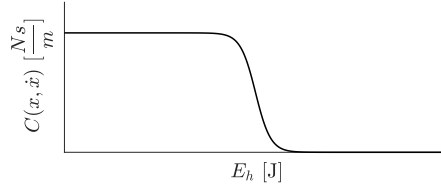
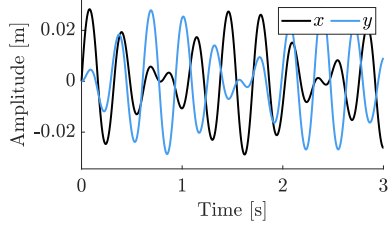


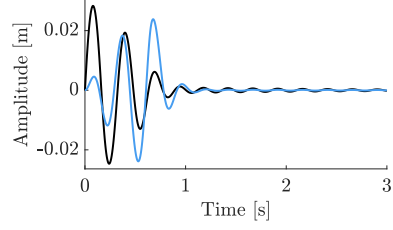
Fig. 22: Controller damping factor based on energy in host system

6.4 Results

The results of the tuning of n without and with dissipation strategy are shown in Figure 23. These figures also clarify the different steps in this control strategy. First, energy transfer between host and controller is induced (Fig. 23a), then, dissipation is added (Fig. 23b). The authors recognise that an in-depth investigation and optimisation of the energy dissipation strategy is needed, however, this is outside the scope of this work.



(a) Results of tuned controller for energy transfer



(b) Results of tuned controller with energy dissipation

Fig. 23: Resulting time responses of host system and controller coordinate, for controller tuned to example system from [31]

6.5 Deviation of softening stiffness model

The model of the nonlinear stiffness of the host system given in [31], differs from the arctangent nonlinearity considered in this work. To observe how the control strategy deals with this deviating stiffness of the host, simulations are done with the following nonlinear elastic force characteristic.

$$K_0(x) = k \frac{(L_0 - \sqrt{H^2 + x^2})x}{\sqrt{H^2 + x^2}} \quad (25)$$

Here k , L_0 and H are fixed constants. In the regarded case, $k = 50 \frac{N}{m}$, $L_0 = 0.07m$ and $H = 0.028m$ [31]. Note that the controller remains unchanged compared to the above results, while the host system has a new stiffness expression $K_0(x)$. The comparison of the nonlinear stiffness $K_0(x)$ (Eq. (25)) and the arctangent stiffness considered in Sections 6.1-6.4 is shown in Fig. 24. Note that K_0 is still a softening stiffness, however, the monotonicity is lost.

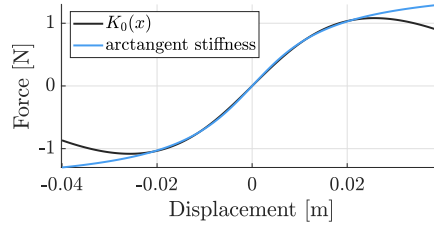
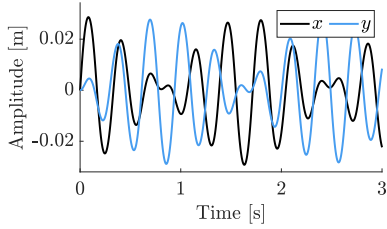
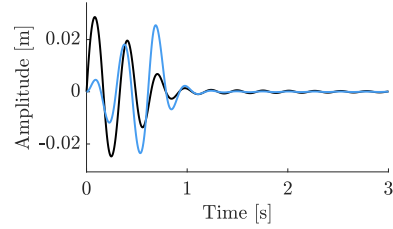


Fig. 24: Comparison of arctangent stiffness characteristic and K_0

The resulting time responses are shown in Fig. 25. These results show that the proposed control strategy can deal with the different softening nonlinearity.



(a) Results of tuned controller for energy transfer



(b) Results of tuned controller with energy dissipation

Fig. 25: Resulting time responses of host system and controller coordinate, for controller tuned to example system from [31], with host stiffness defined by Eq. (25)

7 Conclusion

This work investigated the active vibration control of a nonlinear system with a softening spring, excited by an impulsive load. The Virtual Mechanical System control law was applied, which aims to control energy flows. This control law describes an auxiliary system, which is coupled to the host skew-symmetrically with coupling parameter n . This coupling, typical for gyroscopic systems, creates a 90° phase shift between the host system and controller system, and facilitates energy transfer. Due to the passivity, semi-analytical techniques can be employed. By analysing the slow flow behaviour of the controlled system, insight into the tuning of n is achieved. Bifurcations in the system of slow flow equations are translated into a threshold value n_c for energy transfer to the controller. Further, the influence of varying n ($> n_c$) on the speed of energy transfer and the beat quality is discussed. Using these insights, n can be tuned to ensure efficient energy transfer from the system towards the controller, whereafter, different strategies for dissipation in the controller can be applied. This way, vibration control is achieved. The practical example provided illustrates the tuning strategy in a practical manner. Furthermore, the results with a different nonlinear stiffness characteristic illustrate the broader applicability of the proposed approach.

Ultimately, the analytical insights into the controller tuning allow for a profound understanding of the energy transfer phenomenon for systems with softening stiffness and deepen our understanding of the VMS control law and its skew-symmetric coupling.

Acknowledgements. This work was supported by the research Foundation Flanders - FWO in the form of a PhD Fellowship fundamental research [grant number 1147925N] and by a BOF postdoctoral fellowship [grant number 01P02222].

Declarations

The authors declare that they have no conflict of interest.

References

- [1] Mahmoud, G.M., Bountis, T.: The dynamics of systems of complex nonlinear oscillators: A review. *International Journal of Bifurcation and Chaos* **14**(11), 3821–3846 (2004) <https://doi.org/10.1142/S0218127404011624>
- [2] Goh, C.J., Caughey, T.K.: On the stability problem caused by finite actuator dynamics in the collocated control of large space structures. *International Journal of Control* **41**(3), 787–802 (1985) <https://doi.org/10.1080/0020718508961163>
- [3] Loria, A., Nijmeijer, H.: *Passivity based control. Encyclopedia of life support systems*. EOLSS publishers, Oxford (2004)
- [4] Hao, S., Yamashita, Y., Kobayashi, K.: Passivity-based control of nonlinear active dynamic vibration absorber. *International Journal of Robust and Nonlinear Control* **33**(5), 3247–3266 (2023) <https://doi.org/10.1002/rnc.6584> <https://onlinelibrary.wiley.com/doi/pdf/10.1002/rnc.6584>
- [5] Chesné, S.: Hybrid skyhook mass damper. *Mechanics & Industry* **22**, 49 (2021) <https://doi.org/10.1051/meca/2021050>
- [6] Chan-Zheng, C., Muñoz-Arias, M., Scherpen, J.M.A.: Tuning rules for passivity-based integral control for a class of mechanical systems. *IEEE Control Systems Letters* **7**, 37–42 (2023) <https://doi.org/10.1109/LCSYS.2022.3186618>
- [7] Feliu, V., Pereira, E., Díaz, I.M.: Passivity-based control of single-link flexible manipulators using a linear strain feedback. *Mechanism and Machine Theory* **71**, 191–208 (2014) <https://doi.org/10.1016/j.mechmachtheory.2013.07.009>
- [8] Liu, L.-Y., Yuan, K.: Noncollocated passivity-based pd control of a single-link flexible manipulator. *Robotica* **21**(2), 117–135 (2003) <https://doi.org/10.1017/S0263574702004538>
- [9] Juchem, J., Geyskens, S., Dekemele, K., Loccufier, M.: A virtual mechanical system control law for energy transfer towards a single actuation point in n dof buildings. *Engineering Structures* **302**, 117493 (2024) <https://doi.org/10.1016/j.engstruct.2024.117493>
- [10] Luyckx, L. and Loccufier, M. and Noldus, E.: On the design of nonlinear controllers for Euler-Lagrange systems. *Nonlinear Dynamics and Systems Theory* **1**(1), 97–107 (2001)
- [11] Li, X., Sun, K., Liu, H.: A modified constant-torque spring hinge toward synchronous deployment. *Advances in Space Research* **70**(11), 3301–3310 (2022) <https://doi.org/10.1016/j.asr.2022.08.005>

- [12] Li, X., Sun, K., Liu, H.: A modified constant-torque spring hinge toward synchronous deployment. *Advances in Space Research* **70**(11), 3301–3310 (2022) <https://doi.org/10.1016/j.asr.2022.08.005>
- [13] Liu, C.-H., Chung, F.-M., Ho, Y.-P.: Topology optimization for design of a 3d-printed constant-force compliant finger. *IEEE/ASME Transactions on Mechatronics* **26**(4), 1828–1836 (2021) <https://doi.org/10.1109/TMECH.2021.3077947>
- [14] Wang, J.-Y., Lan, C.-C.: A constant-force compliant gripper for handling objects of various sizes. *Journal of Mechanical Design* **136**(7), 071008 (2014) <https://doi.org/10.1115/1.4027285>
- [15] Lo, C.-W., Chang, Y., Wang, M.-L., Lee, J.-J.: Design of a large stroke compliant gripping mechanism for constant-force applications. *Journal of the Brazilian Society of Mechanical Sciences and Engineering* **46**(6), 363 (2024) <https://doi.org/10.1007/s40430-024-04929-4>
- [16] Ding, B., Zhao, J., Li, Y.: Design of a spatial constant-force end-effector for polishing/deburring operations. *The International Journal of Advanced Manufacturing Technology* **116**(11), 3507–3515 (2021) <https://doi.org/10.1007/s00170-021-07579-1>
- [17] Dekemele, K., Habib, G.: Inverted resonance capture cascade: modal interactions of a nonlinear energy sink with softening stiffness. *Nonlinear Dynamics* **111**(11), 9839–9861 (2023) <https://doi.org/10.1007/s11071-023-08423-9>
- [18] Zhang, S., Zhou, J., Ding, H., Wang, K., Tan, D.: Theoretical investigation on vibration mitigation in a system with fractional nonlinear energy sinks. *Nonlinear Dynamics* (2024) <https://doi.org/10.1007/s11071-024-10557-3>
- [19] Qaiser, Z., Johnson, S., Rehman, T., Shun, B., Zhou, Y.: Order-of-magnitude increased range of constant force adjustment via section optimization. *Mechanism and Machine Theory* **205**, 105835 (2025) <https://doi.org/10.1016/j.mechmachtheory.2024.105835>
- [20] Li, J., Rehman, T.U., Qaiser, Z., Johnson, S.: Design optimization and validation of compliant bidirectional constant force mechanisms. *Mechanism and Machine Theory* **195**, 105593 (2024) <https://doi.org/10.1016/j.mechmachtheory.2024.105593>
- [21] Phan, T.-V., Pham, H.-T.: Design and optimization of a large-stroke compliant constant-torque mechanism. *Journal of Technical Education Science*, 93–100 (2022) <https://doi.org/10.54644/jte.68.2022.1098>
- [22] Habib, G., Kerschen, G.: A principle of similarity for nonlinear vibration absorbers. *Physica D: Nonlinear Phenomena* **332**, 1–8 (2016) <https://doi.org/10.1016/j.physd.2016.06.001>

- [23] Habib, G., Kádár, F., Papp, B.: Impulsive vibration mitigation through a nonlinear tuned vibration absorber. *Nonlinear Dynamics* **98** (2019) <https://doi.org/10.1007/s11071-019-05312-y>
- [24] Manevich, A.I., Manevitch, L.I.: *The Mechanics of Nonlinear Systems with Internal Resonances*. Published by Imperial College Press and distributed by World Scientific Publishing Co., Singapore (2005). <https://doi.org/10.1142/p368>
- [25] Quinn, D.D., Gendelman, O., Kerschen, G., Sapsis, T.P., Bergman, L.A., Vakakis, A.F.: Efficiency of targeted energy transfers in coupled nonlinear oscillators associated with 1:1 resonance captures: Part i. *Journal of Sound and Vibration* **311**(3), 1228–1248 (2008) <https://doi.org/10.1016/j.jsv.2007.10.026>
- [26] Petit, F., Loccufer, M., Aeyels, D.: The energy thresholds of nonlinear vibration absorbers. *Nonlinear Dynamics* **74** (2013) <https://doi.org/10.1007/s11071-013-1003-8>
- [27] Genta, G.: *Dynamics of Rotating Systems*. Springer, New York, NY (2005)
- [28] Strogatz, S.H.: *Nonlinear Dynamics and Chaos: With Applications to Physics, Biology, Chemistry, and Engineering*. CRC Press, Taylor & Francis Group, Boca Raton, FL 33487-2742 (2018). <https://books.google.be/books?id=A0paDwAAQBAJ>
- [29] Wiebe, R., Virgin, L.: A heuristic method for identifying chaos from frequency content. *Chaos (Woodbury, N.Y.)* **22**, 013136 (2012) <https://doi.org/10.1063/1.3675624>
- [30] Juchem, J.: *The virtual mechanical system controller: Vibration mitigation for underactuated mechanical systems*. Phd thesis, Ghent University, Ghent, BE (September 2024)
- [31] Tommasino, D., Cipriani, G., Doria, A., Rosati, G.: Effect of end-effector compliance on collisions in robotic teleoperation. *Applied Sciences* **10**(24) (2020) <https://doi.org/10.3390/app10249077>